

2403 **Chapter 9**
2404 **Weak Focusing Synchrotron**

2405 **Abstract** This Chapter introduces to the weak focusing synchrotron, and to the the-
2406 oretical material needed for the simulation exercises. It begins with a brief reminder
2407 of the historical context, and continues with beam optics and acceleration techniques
2408 which the weak synchrotron principle and methods lean on. Regarding the latter, it
2409 relies on basic charged particle optics and acceleration concepts introduced in the
2410 previous Chapters, and further addresses the following aspects:

- 2411 - fixed closed orbit,
- 2412 - periodic structure,
- 2413 - periodic motion stability,
- 2414 - optical functions,
- 2415 - synchrotron motion,
- 2416 - depolarizing resonances.

2417 The simulation of weak synchrotrons only require a very limited number of optical
2418 elements; actually two are enough: DIPOLE or BEND to simulate combined function
2419 dipoles, and DRIFT to simulate straight section. A third one CAVITE, is required
2420 for acceleration. Particle monitoring requires keywords introduced in the previous
2421 Chapters, including FAISCEAU, FAISTORE, possibly PICKUPS, and some others.
2422 Spin motion computation and monitoring resort to SPNTRK, SPNPRT, FAISTORE.
2423 Optics matching and optimization use FIT[2]. SYSTEM again is used to shorten the
2424 input data files.

2425 Notations used in the Text

$B; \mathbf{B}, B_{x,y,s}$	field value; field vector, its components in the moving frame
$B\rho = p/q; B\rho_0$	particle rigidity; reference rigidity
$C; C_0$	orbit length, $C = 2\pi R + \left[\begin{array}{l} \text{straight} \\ \text{sections} \end{array} \right]$; reference, $C_0 = C(p = p_0)$
E	particle energy
EFB	Effective Field Boundary
$f_{\text{rev}}, f_{\text{rf}}$	revolution and accelerating voltage frequencies
h	RF harmonic number, $h = f_{\text{rf}}/f_{\text{rev}}$
$m; m_0; M$	mass, $m = \gamma m_0$; rest mass; in units of MeV/c ²
$n = \frac{\rho}{B} \frac{dB}{d\rho}$	focusing index
$\mathbf{p}; p; p_0$	momentum vector; its modulus; reference
P_i, P_f	polarization, initial, final
q	particle charge
r, R	orbital radius ; average radius, $R = C/2\pi$
s	path variable
v	particle velocity
$V(t); \hat{V}$	oscillating voltage; its peak value
x, x', y, y'	horizontal and vertical coordinates in the moving frame
α	momentum compaction, or trajectory deviation
$\beta = v/c; \beta_0; \beta_s$	normalized particle velocity; reference; synchronous
β_u	betatron functions (u: x, y, Y, Z)
$\gamma = E/m_0$	Lorentz relativistic factor
$\Delta p, \delta p$	momentum offset
ϵ_u	Courant-Snyder invariant (u: x, r, y, l, Y, Z, s, etc.)
ϵ_R	strength of a depolarizing resonance
ρ	curvature radius
$\phi; \phi_s$	particle phase at voltage gap; synchronous phase
ϕ_u	betatron phase advance, $\phi_u = \int ds/\beta_u$ (u: x, y, Y, or Z)
φ	spin angle to the vertical axis

2427 Introduction

2428 The synchrotron is an outcome of the mid-1940s longitudinal phase focusing syn-
 2429 chronous acceleration concept [1, 2]. In its early version, transverse beam stability
 2430 during acceleration was based on the technique known at the time: weak focusing, as
 2431 in the cyclotron and in the betatron. An existing betatron was used to first demonstrate
 2432 phase-stable synchronous acceleration with slow variation of the magnetic field, on
 2433 a fixed orbit, in 1946 [3], - closely following the demonstration of the principle of
 2434 phase focusing using a fixed-field cyclotron [4].

2435 Phase focusing states that stability of the longitudinal motion, longitudinal focus-
 2436 ing, is obtained if particles in a bunch arrive at the accelerating gap in the vicinity
 2437 of a proper phase of the oscillating voltage, the synchronous phase; if this condition
 2438 is fulfilled the bunch stays together, in the vicinity of the latter, during acceleration.
 2439 Synchrotrons are in general non-isochronous cyclic accelerators: the revolution
 2440 period changes with energy; as a consequence, in order to maintain an accelerated
 2441 bunch on the synchronous phase, the RF voltage frequency, which satisfies
 2442 $f_{rf} = hf_{rev}$, has to change continuously from injection to top energy. The reference
 2443 orbit in a synchrotron is maintained at constant radius by ramping the guiding field
 2444 in the main dipoles in synchronism with the acceleration, as in the betatron [5].

2445 The synchrotron concept allowed the highest energy reach by particle accelerators
 2446 at the time, it led to the construction of a series of proton rings with increasing energy:
 2447 1 GeV at Birmingham (1953), 3.3 GeV at the Cosmotron (Brookhaven National
 2448 Laboratory, 1953), 6.2 GeV at the Bevatron (Berkeley, 1954), 10 GeV at the Synchro-
 2449 Phasotron (JINR, Dubna, 1957, operated until 2003), and a few additional ones in
 2450 the late 1950s well into the era of the concept which would essentially dethrone the
 2451 weak focusing method and its quite bulky rings of magnets which were a practical
 2452 limit to further increase in energy¹: the strong focusing synchrotron (the object of
 2453 Chapter 10). The general layout of these first weak focusing synchrotrons included
 2454 straight sections (often 4, Fig. 9.1), which allowed insertion of injection (Fig. 9.1)
 2455 and extraction systems, accelerating cavities, orbit correction and beam monitoring
 2456 equipment.

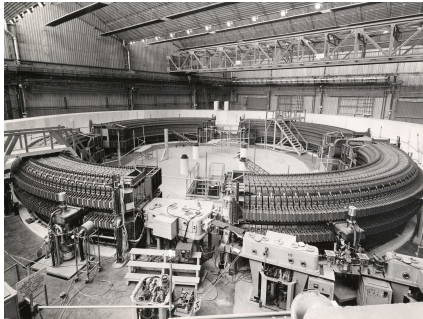


Fig. 9.1 Saturne I at Saclay [6], a 3 GeV, 4-period, 68.9 m circumference, weak focusing synchrotron, constructed in 1956-58. The injection line can be seen in the foreground, injection is from a 3.6 MeV Van de Graaff (not visible)

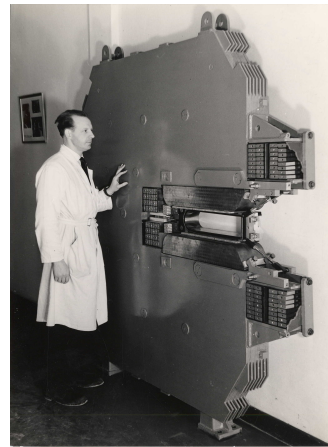


Fig. 9.2 A slice of Saturne I weak focusing synchrotron dipole [7], with its hardly visible gap tapering (greater outward) to satisfy the weak index condition $0 < n < 1$

¹ The sorry has it that it is possible to ride a bicycle in the vacuum chamber of Dubna's Synchro-Phasotron.

2457 9.1 Basic Concepts and Formulæ

2458 The synchrotron is based on two key principles: (i) a slowly varying magnetic field
2459 to maintain an accelerated particle, with momentum $p(t)$, on a constant arc, with
2460 radius ρ , in the bending dipoles, namely,

$$B(t) \times \rho = p(t)/q, \quad \rho = \text{constant}, \quad (9.1)$$

2461 and (ii) synchronous acceleration and longitudinal phase stability. In a regime where
2462 the velocity change with energy cannot be ignored (non-ultrarelativistic particles),
2463 the latter requires a modulation of the accelerating voltage frequency so to satisfy

$$f_{RF}(t) = hf_{rev}(t) \quad (9.2)$$

2464 Synchronism between RF voltage oscillation and the revolution motion keeps the
2465 bunch on the synchronous phase at traversal of the accelerating gaps. Synchronous
2466 acceleration is technologically simpler in the case of electrons, as frequency mod-
2467 ulation is unnecessary beyond a few MeV; for instance, from $v/c = 0.9987$ at
2468 10 MeV to $v/c \rightarrow 1$ the relative change in revolution frequency amounts to
2469 $\delta f_{rev}/f_{rev} = \delta\beta/\beta < 0.0013$.

2470 These are two major evolutions compared to the cyclotron, where, instead, the
2471 magnetic field is fixed - the reference orbit spirals out, and, by virtue of the isochro-
2472 nism of the orbits, the oscillating voltage frequency is fixed as well.

2473 A fixed orbit reduces the radial extent of individual guiding magnets, allowing a
2474 ring structure comprised of a circular string of dipoles. For the sake of comparison:
2475 a synchrocyclotron instead uses a single, massive dipole; increased energy requires
2476 increased radial extent of the magnet to allow for the greater bending field integral
2477 (i.e., $\oint B dl = 2\pi R_{max} \hat{B} = p_{max}/q$), thus a volume of iron increasing more than
2478 quadratically with bunch rigidity.

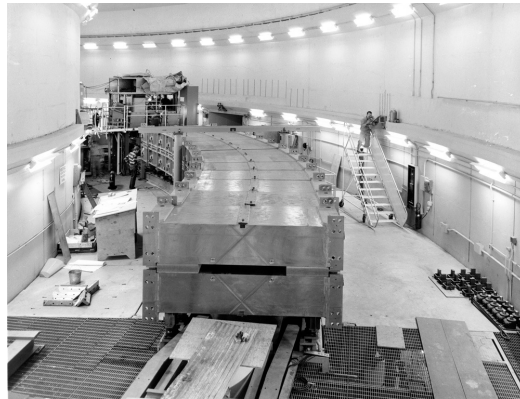
2479 One or the other of the weak field index technique ($-1 < k < 0$, Sect. 4.2.2)
2480 and wedge focusing (Sect. 18.3.1) are used in weak field synchrotrons. Transverse
2481 stability was based on the latter at Argonne ZGS (Zero-Gradient Synchrotron: the
2482 main magnet had no field index), a 12 GeV, 8-dipole, 4-period ring, operated over
2483 1964-1979 (Fig. 9.3). ZGS was the first synchrotron to accelerate polarized proton
2484 beams, from July 1973 on [8].

2485 Due to the necessary ramping of the field in order to maintain a constant orbit,
2486 the synchrotron is a pulsed accelerator, the acceleration is cycled, from injection to
2487 top energy, repeatedly. The repetition rate of the acceleration cyclic depends on the
2488 type of power supply. If the ramping uses a constant electromotive force ($E=V+ZI$
2489 is constant), then

$$B(t) \propto (1 - e^{-\frac{t}{\tau}}) = 1 - \left[1 - \left(\frac{t}{\tau}\right) + \left(\frac{t}{\tau}\right)^2 - \dots \right] \approx \frac{t}{\tau} \quad (9.3)$$

2490 essentially linear. In that case $\dot{B} = dB/dt$ does not exceed a few Tesla/second, thus
2491 the repetition rate of the acceleration cycle if of the order of a Hertz. If instead the

Fig. 9.3 The ZGS at Argonne during construction. A 12 GeV, 8-dipole, 4-period, 172 m circumference, wedge focusing synchrotron. The two persons inside and outside the ring, in the background, give an idea of the size of the magnets



2492 magnet winding is part of a resonant circuit the field law has the form

$$B(t) = B_0 + \frac{\hat{B}}{2}(1 - \cos \omega t) \quad (9.4)$$

2493 so that, in the interval of half a voltage repetition period (*i.e.*, $t : 0 \rightarrow \pi/\omega$), the
 2494 field increases from an injection threshold value to a maximum value at highest
 2495 rigidity, $B(t) : B_0 \rightarrow B_0 + \hat{B}$. The latter determines the highest achievable energy:
 2496 $\hat{E} = pc/\beta = q\hat{B}\rho c/\beta$. The repetition rate with resonant magnet cycling can reach
 2497 a few tens of Hertz, a species known as “rapid-cycling” synchrotrons. In both cases
 2498 anyway B imposes its law and the other quantities comprising the acceleration cycle
 2499 (RF frequency in particular) will follow B(t).

2500 For the sake of comparison again: in a synchrocyclotron the field is constant,
 2501 thus acceleration can be cycled as fast as the swing of the voltage frequency allows
 2502 (hundreds of Hz are common practice); assume a conservative 10 kVolts per turn,
 2503 thus of the order of 10,000 turns to 100 MeV, with velocity $0.046 < v/c < 0.43$
 2504 from 1 to 100 MeV, proton. Take $v \approx 0.5c$ to make it simple, an orbit circumference
 2505 below 30 meter, thus the acceleration takes of the order of $10^4 \times C/0.5c \approx \text{ms}$ range,
 2506 potentially a repetition rate in kHz range, more than an order of magnitude beyond
 2507 the reach of a rapid-cycling pulsed synchrotron.

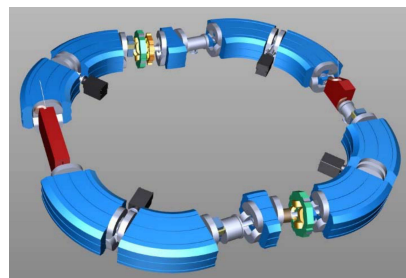


Fig. 9.4 A recent design of a zero-gradient wedge focusing synchrotron for hadrontherapy application [9]

2508 The next decades following the invention of the synchrotron saw applications in
 2509 many fields of science including fixed-target nuclear physics for particle discovery,
 2510 material science, medicine, industry. Its technological simplicity still makes it an
 2511 appropriate technology today in low energy beam application when relatively low
 2512 beam current is not a concern, as in the hadrontherapy application (Fig. 9.4) [9]: it
 2513 essentially requires a single type of a simple dipole magnet, an accelerating gap, some
 2514 command-control instrumentation, whereas it procures greater beam manipulation
 2515 flexibilities compared to (synchro-)cyclotrons.

2516 9.1.1 Periodic Stability

2517 This section addresses transverse focusing and periodic stability in a weak focusing
 2518 synchrotron. It builds on material introduced in Chap. 4, Classical Cyclotron, and
 2519 on material drawn from Ref. [13].

2520 9.1.1.1 Closed orbit

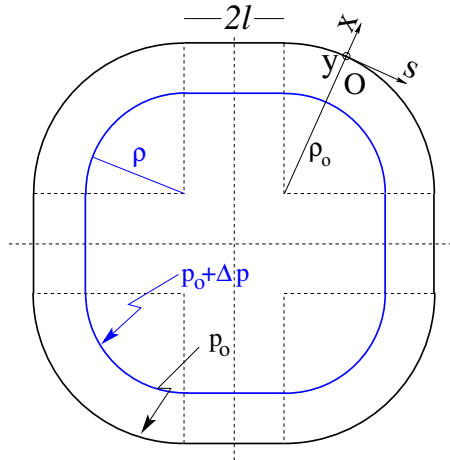
2521 The concept is that of the betatron, which accelerates particles on a constant orbit
 2522 (Chap. 7). Bunches accelerated in a synchrotron follow a closed orbit: at any azimuth
 2523 around the ring, the closed orbit is the average position of the particles, turn after
 2524 turn. The closed orbit is fixed, and maintained during acceleration by ensuring that
 2525 the relationship Eq. 9.1 is satisfied. In a perfect ring, the closed orbit is along a
 2526 reference arc in the bending magnets, continuing in a straight line in the drift spaces
 2527 between dipoles, Fig. 9.5; this sequence of connected curves and straights defines a
 2528 reference orbit.

2529 Particle motion is defined in a moving frame (O;s,x,y) whose origin coincides with
 2530 the location of a reference particle following the reference orbit. The moving frame s
 2531 axis is tangent to the reference orbit, its transverse horizontal axes x is normal to the
 2532 s axis, its vertical axis y is normal to the (s, x) plane (Fig. 4.8, Sect. 4.2.2).

2533 9.1.1.2 Transverse Focusing

2534 Radial motion stability around a reference closed orbit in an axially symmetric dipole
 2535 field requires the geometrical configuration of particle orbits sketched in Fig. 9.6,
 2536 resulting from magnetic rigidity $B \times \rho$ an increasing function of radius, which, on
 2537 the closed orbit (radius = ρ_0), expresses as $\frac{\partial B \rho}{\partial \rho} \geq 0$, viz. $1 + \frac{\rho}{B_0} \frac{\partial B}{\partial \rho} \geq 0$. Vertical
 2538 stability requires the gap height to increase with radius, thus field decreases with
 2539 radius, $\frac{\partial B_y}{\partial \rho} < 0$ (Fig. 4.9, Sec. 4.2.2). This is the focusing method which was used
 2540 in the classical cyclotron and results in the typical magnet slice shown in Fig. 9.2.
 2541 Introduce the field index

Fig. 9.5 A $2\pi/4$ axially symmetric structure with four drift spaces. Orbit length on reference momentum p_0 is $C = 2\pi\rho_0 + 8l$. (O; s, x, y) is the moving frame, along the reference orbit. The orbit for momentum $p = p_0 + \Delta p$ ($\Delta p < 0$, here) is at constant distance $\Delta x = \frac{\rho_0}{1-n} \frac{\Delta p}{p_0} = \frac{R}{(1+k)(1-n)} \frac{\Delta p}{p_0}$ from the reference orbit



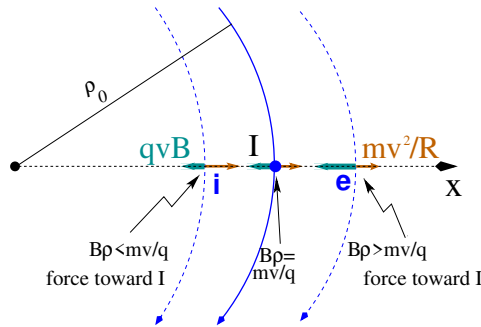
$$n = -\frac{\rho_0}{B_0} \left. \frac{\partial B_y}{\partial \rho} \right|_{x=0, y=0} \tag{9.5}$$

2542 Note the sign convention from now on, the opposite sign to the cyclotron case
 2543 (Eq. 4.10). Transverse motion stability in an axially symmetric structure, with or
 2544 without drift spaces, thus summarizes in

$$0 < n < 1 \tag{9.6}$$

Adding drift spaces between dipoles, the reference orbit is comprised of arcs of

Fig. 9.6 Radial motion stability in an axially symmetric structure. The resultant $F_i = -qvB + mv^2/r$, is zero at I: $B_0\rho_0 = mv/q$. The resultant at i is toward I if $qvB_i < mv^2/\rho_i$, i.e. $B_i\rho_i < mv/q$; the resultant at e is toward I if $qvB_e > mv^2/\rho_e$, i.e. $B_e\rho_e > mv/q$



2545 radius ρ_0 in the magnets, and straight segments along the drift spaces that connect
 2546 these arcs. It requires defining two radii, namely,
 2547 (i) the magnet curvature radius ρ_0 (Fig. 9.7),
 2548

2549 (ii) an average radius $R = C/2\pi = \rho_0 + Nl/\pi$ (with C the length of the reference
2550 closed orbit and $2l$ the drift length) (Fig. 9.5) which also writes

$$R = \rho_0(1 + k), \quad k = \frac{Nl}{\pi\rho_0} \quad (9.7)$$

2551 Adding drift spaces decreases the average focusing around the ring. Trajectories of
2552 different momenta are parallel (Figs. 9.7, 9.5).

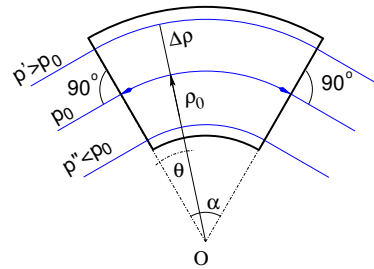


Fig. 9.7 In a sector dipole with radial index $n \neq 0$, closed orbits follow arcs of constant B . A closed orbit at $p_0 + \Delta p$ follows an arc of radius $\rho_0 + \Delta\rho$, $\Delta\rho = \Delta p / (1 + n)qB_0$

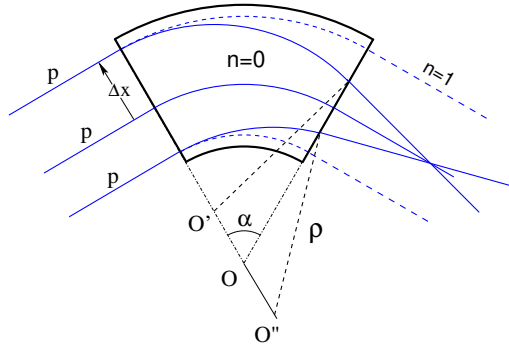
2553 Geometrical focusing

2554 The limit $n \rightarrow 1$ of the transverse motion stability domain corresponds to a cancel-
2555 lation of the geometrical focusing (Fig. 9.8): in a constant field dipole (radial field
2556 index $n=0$) the longer (respectively shorter) path in the magnetic field for parallel
2557 trajectories entering the magnet at greater (respectively smaller) radius result in
2558 convergence. This effect is cancelled, *i.e.*, the deviation is the same whatever the
2559 entrance radius, if the curvature center is made independent of the entrance radius:
2560 $OO' = 0$, $O''O = 0$. This occurs if trajectories at an outer (inner) radius experience a
2561 smaller (greater) field such as to satisfy $BL = B\rho\alpha = C^{st}$. Differentiating $B\rho = C^{st}$
2562 gives $\frac{\Delta B}{B} + \frac{\Delta\rho}{\rho} = 0$, with $\Delta\rho = \Delta x$, so yielding $n = -\frac{\rho_0}{B_0} \frac{\Delta B}{\Delta x} = 1$. The focal distance
2563 associated with the curvature is (Eq. 4.12 with $R = \rho_0$) $f = \frac{\rho_0^2}{L}$. Optical drawbacks
2564 of the weak focusing method are, the weakness of the focusing and the absence of
2565 independent radial and axial focusing.

2566 Wedge Focusing

2567 Profiling the magnet gap in order to adjust the focal distance complicates the magnet;
2568 $n=0$, a parallel gap, makes it simpler. Entrance and exit wedge angles may then be
2569 used (Fig. 18.8): opening the magnetic sector increases the horizontal focusing (and
2570 decreases the vertical focusing); closing the magnetic sector has the reverse effect.

Fig. 9.8 Geometrical focusing: in a sector dipole with focusing index $n = 0$, parallel incoming rays of equal momenta experience the same curvature radius ρ , they exit converging, as a result of the longer path of outer trajectories in the field, compared to inner ones. An index value $n=1$ cancels that effect: rays exit parallel



2571 *Vertical focusing at the EFB*

2572 The magnetic field falls off smoothly in the fringe field region at the ends of a magnet,
 2573 from its value in the body to zero at some distance from the iron. The extent of the
 2574 fall-off is commensurate with the gap size, its shape depends on such factors as the
 2575 profiling of the iron at the EFB (Fig. 9.9) or the positioning and shape of the coils.

2576 From an optics standpoint, the main effect of the fringe field is the existence of a
 2577 longitudinal component of the field, $\mathbf{B}_s(s)$. In a mid-plane symmetry dipole, $\mathbf{B}_s(s)$
 2578 is non-zero off the median plane, and normal to the iron (Fig. 9.9).

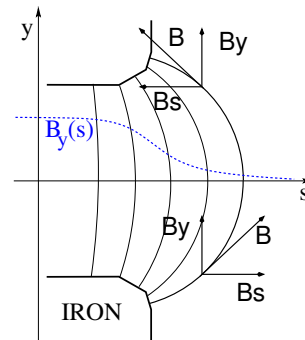


Fig. 9.9 Field components in the $B_y(s)$ fringe field region at a dipole EFB

2579 The focal distance f associated with a wedge angle ϵ (Fig. 18.8) satisfies

$$\frac{1}{f} = \tan \frac{\epsilon}{\rho_0} \tag{9.8}$$

2580 with $\epsilon > 0$ if the sector is closing, by convention. In a point transform approximation,
 2581 at the wedge the trajectory undergoes a local deviation proportional to the distance
 2582 to the optical axis, namely,

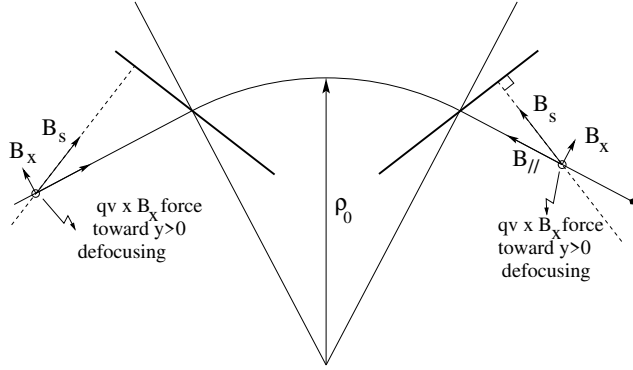


Fig. 9.10 Field components in the fringe field region at the end of a dipole ($y > 0$, here, referring to Fig. 9.9). $B_{//}$ is parallel to the particle velocity. This configuration is vertically defocusing: a charged particle traveling off mid-plane is pulled away from the the latter under the effect of $\mathbf{v} \times \mathbf{B}_x$ force component. Inspection of the $y < 0$ region gives the same result: the charge is pulled away from the median plane

$$\Delta x' = \frac{\tan \epsilon}{\rho_0} \Delta x, \quad \Delta y' = -\frac{\tan \epsilon}{\rho_0} \Delta y \quad (9.9)$$

2583 Wedge vertical focusing in the ZGS ($\epsilon > 0$) was at the expense of horizontal
 2584 geometrical focusing (Fig. 9.7). This was an advantage though for the acceleration
 2585 of polarized beams, as radial field components (which are responsible for depolarization)
 2586 were only met at the EFBs of the eight main dipoles [8]. Preserving beam
 2587 polarization at high energy required tight control of the tunes, and this was achieved
 2588 by, in addition, pole face winding at the ends of the dipoles [10, 11]; these coils
 2589 where pulsed to control amplitude detuning, resulting in tune control at 0.01 level,
 2590 they also compensated eddy currents induced sextupole perturbations affecting the
 2591 vertical tune.

2592 *Fringe field extent*

2593 The fringe field extent, say λ , may be taken into account in the thin lens approximation
 2594 of the wedge focusing. It only modifies the horizontal focusing to the second order
 2595 in the coordinates, but changes the vertical focusing to the first order, namely

$$\Delta x' = \frac{\tan \epsilon}{\rho_0} \Delta x, \quad \Delta y' = -\frac{\tan(\epsilon - \psi)}{\rho_0} \Delta y \quad (9.10)$$

2596 wherein

$$\psi = I_1 \frac{\lambda}{\rho_0} \frac{1 + \sin^2 \epsilon}{\cos \epsilon}, \quad \text{with } I_1 = \int_{s(B=0)}^{s(B=B_0)} \frac{B(s)(B_0 - B(s)) ds}{B_0^2 \lambda} \quad (9.11)$$

2597 and the integral I_1 extends over the field fall-off where B evolves between 0 to a
2598 plateau value B_0 inside the magnet.

2599 9.1.1.3 Periodic stability, betatron motion

2600 The first order differential equations of motion in the Serret-Frénet frame (Fig. 9.5)
2601 derive from the Lorentz equation [13]

$$\frac{d\mathbf{m}\mathbf{v}}{dt} = q\mathbf{v} \times \mathbf{B} \Rightarrow m \frac{d}{dt} \begin{Bmatrix} \frac{ds}{dt} \mathbf{s} \\ \frac{dx}{dt} \mathbf{x} \\ \frac{dy}{dt} \mathbf{y} \end{Bmatrix} = q \begin{Bmatrix} (\frac{dx}{dt} B_y - \frac{dy}{dt} B_x) \mathbf{s} \\ -\frac{ds}{dt} B_y \mathbf{x} \\ \frac{ds}{dt} B_x \mathbf{y} \end{Bmatrix} \quad (9.12)$$

2602 Introduce the field index $n = -\frac{\rho_0}{B_0} \frac{\partial B_y}{\partial x}$ evaluated on the reference orbit, with $B_0 =$
2603 $B_y(\rho_0, y = 0)$; assume transverse stability: $0 < n < 1$. Taylor expansion of the field
2604 components in the moving frame write

$$B_y(\rho) = B_y(\rho_0) + x \left. \frac{\partial B_y}{\partial x} \right|_{\rho_0} + \mathcal{O}(x^2) \approx B_y(\rho_0) - n \frac{B_y}{\rho_0} \Big|_{\rho_0} x = B_0 \left(1 - n \frac{x}{\rho_0}\right)$$

$$B_x(0+y) = \underbrace{B_x(0)}_{=0} + y \underbrace{\left. \frac{\partial B_x}{\partial y} \right|_{\rho_0}}_{=\frac{\partial B_y}{\partial x}} (+ \text{higher order in } y) \approx -n \frac{B_0}{\rho_0} y \quad (9.13)$$

2605 Introduce in addition $ds \approx v dt$, Eqs. 9.12, 9.13 lead to the differential equations of
2606 motion in a dipole field

$$\frac{d^2 x}{ds^2} + \frac{1-n}{\rho_0^2} x = 0, \quad \frac{d^2 y}{ds^2} + \frac{n}{\rho_0^2} y = 0 \quad (0 < n = \frac{\rho_0}{B_0} \frac{\partial B_y}{\partial x} < 1) \quad (9.14)$$

2607 It results that, in an S-periodic structure comprised of dipoles, wedges and drift
2608 spaces, the differential equation of motion takes the general form of Hill's equation, a
2609 second order differential equation with periodic coefficient, namely (with z standing
2610 for x or y),

$$\begin{cases} \frac{d^2 z}{ds^2} + K_z(s)z = 0 \\ K_z(s+S) = K_z(s) \end{cases} \quad \text{with} \quad \begin{cases} \text{in dipoles : } \begin{cases} K_x = (1-n)/\rho_0^2 \\ K_y = n/\rho_0^2 \end{cases} \\ \text{at a wedge : } K_x = \pm(\tan \epsilon)/\rho_0 \\ \text{in drift spaces : } K_x = K_y = 0 \end{cases} \quad (9.15)$$

2611 $K_z(s)$ is S-periodic, $S = 2\pi R/N$ ($S = C/4$, for instance, in the 4-periodic ring
2612 Saturne 1 (Figs. 9.1, 9.5)). G. Floquet has established [12] that the two independent
2613 solutions of Hill's second order differential equation have the form [13]

$$\left\{ \begin{array}{l} z_1(s) = \sqrt{\beta_z(s)} e^{i \int_0^s \frac{ds}{\beta_z(s)}} \\ dz_1(s)/ds = \frac{i - \alpha_z(s)}{\beta_z(s)} z_1(s) \end{array} \right. \quad \text{and} \quad \left\{ \begin{array}{l} z_2(s) = z_1^*(s) \\ dz_2(s)/ds = dz_1^*(s)/ds \end{array} \right. \quad (9.16)$$

2614 wherein $\beta_z(s)$ and $\alpha_z(s) = -\beta'_z(s)/2$ are S-periodic functions, from what it results
2615 that

$$z_{\frac{1}{2}}(s+S) = z_{\frac{1}{2}}(s) e^{\pm i \mu_z} \quad (9.17)$$

2616 wherein

$$\mu_z = \int_{s_0}^{s_0+S} \frac{ds}{\beta_z(s)} \quad (9.18)$$

2617 is the betatron phase advance over a period. A real solution of Hill's equation is
2618 the linear combination $A z_1(s) + A^* z_2^*(s)$. Take A of the form $A = \frac{1}{2} \sqrt{\varepsilon_z/\pi} e^{i\phi}$
2619 (the introduction of the constant multiplicative factor $\sqrt{\varepsilon_z/\pi}$ is justified below), the
2620 general solution of Eq. 9.15 then takes the form (noting $(*)' = d(*)/ds$)

$$\left\{ \begin{array}{l} z(s) = \sqrt{\beta_z(s) \varepsilon_z/\pi} \cos\left(\int \frac{ds}{\beta_z} + \phi\right) \\ z'(s) = -\sqrt{\frac{\varepsilon_z/\pi}{\beta_z(s)}} \sin\left(\int \frac{ds}{\beta_z} + \phi\right) + \alpha_z(s) \cos\left(\int \frac{ds}{\beta_z} + \phi\right) \end{array} \right. \quad (9.19)$$

2621 The motion coordinates satisfy

$$\frac{1}{\beta_z(s)} [z^2 + (\alpha_z(s)z + \beta_z(s)z')^2] = \frac{\varepsilon_z}{\pi} \quad (9.20)$$

2622 wherein ε_z/π is the so-called Courant-Snyder invariant. At a given azimuth s of the
2623 periodic structure the observed turn-by-turn motion lies on that ellipse (Fig. 9.11).
2624 The form of the ellipse depends on the observation azimuth s via the respective local
2625 values of $\alpha_z(s)$ and $\beta_z(s)$, but its surface ε_z is invariant. Motion along the ellipse
2626 is clockwise, as can be figured from Eq. 9.19 considering an observation azimuth s
2627 where the ellipse is upright, $\alpha_z(s) = 0$.

2628 If a turn is comprised of N periods, the phase advance over a turn (from one
2629 location to the next on the ellipse in Fig. 9.11) is

$$\int_{s_0}^{s_0+NS} \frac{ds}{\beta_z(s)} = N \int_{s_0}^{s_0+S} \frac{ds}{\beta_z(s)} = N \mu_z \quad (9.21)$$

2630 *Weak focusing approximation*

2631 In the case of a cylindrically symmetric structure, a sinusoidal motion is the exact
2632 solution of the first order differential equations of motion (Eqs. 4.14, 4.15, Classical
2633 Cyclotron Chapter). In that case the latter have a constant (s -independent) coefficient,

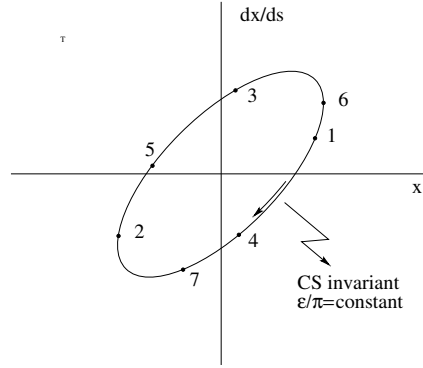


Fig. 9.11 Courant-Snyder invariant and turn-by-turn harmonic motion. The form of the ellipse depends on the observation azimuth s but its surface ε_z is invariant

2634 $K_x = (1 - n)/R_0^2$ and $K_y = n/R_0^2$, respectively. Adding drift spaces results in Hill's
 2635 differential equation with periodic coefficient $K(s + S) = K(s)$ (Eq. 9.15), and in a
 2636 pseudo harmonic solution (Eq. 9.19). Due to the weak focusing the beam envelope
 2637 (Eq. 9.27) is only weakly modulated, thus so is $\beta_z(s)$. In a practical manner, the
 2638 modulation of $\beta_z(s)$ does not exceed a few percent, this justifies introducing the
 2639 average value $\overline{\beta_z}$ to approximate the phase advance by

$$\int_0^s \frac{ds}{\beta_z(s)} \approx \frac{s}{\overline{\beta_z}} = \nu_z \frac{s}{R} \quad (9.22)$$

2640 The right equality is obtained by applying this approximation to the the phase advance
 2641 per period (Eq. 9.29), namely $\mu_z = \int_{s_0}^{s_0+S} \frac{ds}{\beta_z(s)} \approx S/\overline{\beta_z}$, and introducing the wave
 2642 number of the N-period optical structure

$$\nu_z = \frac{N\mu_z}{2\pi} = \frac{\text{phase advance over a turn}}{2\pi} \quad (9.23)$$

2643 so that

$$\overline{\beta_z} = \frac{R}{\nu_z} \quad (9.24)$$

2644 Substituting in Eq. 9.19 results in the approximate solution

$$\begin{cases} z(s) \approx \sqrt{\beta_z(s)\varepsilon_z/\pi} \cos\left(\nu_z \frac{s}{R} + \phi\right) \\ z'(s) = -\sqrt{\frac{\varepsilon_z/\pi}{\beta_z(s)}} \sin\left(\nu_z \frac{s}{R} + \phi\right) + \alpha_z(s) \cos\left(\nu_z \frac{s}{R} + \phi\right) \end{cases} \quad (9.25)$$

2645 In this approximation, the differential equations of motion (Eq. 9.15) can be
 2646 expressed under the form

$$\frac{d^2x}{ds^2} + \frac{\nu_x^2}{R^2}x = 0, \quad \frac{d^2y}{ds^2} + \frac{\nu_y^2}{R^2}y = 0 \quad (9.26)$$

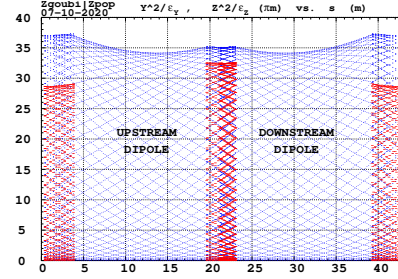
2647 *Beam envelopes*

2648 The beam envelope $\hat{z}(s)$ (with z standing for x or y) is determined by the particle of
 2649 maximum invariant ε_z/π , it is given by

$$\pm\hat{z}(s) = \pm\sqrt{\beta_z(s)\varepsilon_z/\pi} \quad (9.27)$$

As $\beta_z(s)$ is S-periodic, so is the envelope, $\hat{z}(s+S) = \hat{z}(s)$. In a cell with symmetries

Fig. 9.12 ***** rem-
 place par envelope in saturne I
 ***** Beam envelope
 along Saturne I four cells,
 generated by a single particle
 over many turns. The extreme
 excursion at any azimuth s
 tangents the envelope. En-
 velopes along a cell feature
 central symmetry, as does the
 cell



2650 (for instance symmetry with respect to the center of the cell), the envelope features
 2651 the same symmetries. Envelope extrema are at azimuth s where $\beta_z(s)$ is minimum,
 2652 or maximum, *i.e.*, where $\alpha_z = 0$ as $\beta'_z = -2\alpha_z$. This is illustrated in Fig. 9.12. No
 2653 particular hypothesis regarding the amplitude of the motion is required here, it does
 2654 not have to be paraxial and can be arbitrarily large (as long as transverse stability
 2655 still holds).

2656 In the paraxial approximation, envelopes along the optical structure can be deter-
 2657 mined by resorting to matrix transport (*cf.* reminders in Section 19.3.2). An initial
 2658 beam matrix at some azimuth s , as well as the phase advance over a period, can
 2659 be obtained using the stability criterion (Eq. 19.3.3). This is a simple exercise in
 2660 the case of Saturne I type of structure (Figs. 9.1, 9.5). The transport matrix of the
 2661 symmetric drift-dipole-drift cell satisfies
 2662

$$\begin{aligned} [T_{\text{per.}}] &= \begin{bmatrix} 1 & l \\ 0 & 1 \end{bmatrix} \begin{bmatrix} \cos(\sqrt{K_z}\rho_0\alpha) & \frac{1}{\sqrt{K_z}}\sin(\sqrt{K_z}\rho_0\alpha) \\ -\sqrt{K_z}\sin(\sqrt{K_z}\rho_0\alpha) & \cos(\sqrt{K_z}\rho_0\alpha) \end{bmatrix} \begin{bmatrix} 1 & l \\ 0 & 1 \end{bmatrix} \\ &= \begin{bmatrix} \cos(\sqrt{K_z}\rho_0\alpha) - \sqrt{K_z}l\sin(\sqrt{K_z}\rho_0\alpha) & 2l\cos(\sqrt{K_z}\rho_0\alpha) + \frac{1}{\sqrt{K_z}}\sin(\sqrt{K_z}\rho_0\alpha)(1 - K_z l^2) \\ -\sqrt{K_z}\sin(\sqrt{K_z}\rho_0\alpha) & \cos(\sqrt{K_z}\rho_0\alpha) - \sqrt{K_z}l\sin(\sqrt{K_z}\rho_0\alpha) \end{bmatrix} \\ &\approx \begin{bmatrix} \cos\sqrt{K_z}(\rho_0\alpha + l) & 2l\cos(\sqrt{K_z}\rho_0\alpha) + \frac{1}{\sqrt{K_z}}\sin(\sqrt{K_z}\rho_0\alpha) \\ -\sqrt{K_z}\sin(\sqrt{K_z}\rho_0\alpha) & \cos\sqrt{K_z}(\rho_0\alpha + l) \end{bmatrix} \quad (9.28) \end{aligned}$$

2663 The approximation is obtained by assuming that the drift length $2l$ is small compared
 2664 to the arc length $\rho_0\alpha$. From the stability criterion $[T_{\text{per.}}] = I\cos\mu_z + J\sin\mu_z$ it results
 2665 that $\frac{1}{2}\text{Tr}[T_{\text{per.}}] = \cos\mu_z$, which yields the phase advance

$$\mu_z = \sqrt{K_z}(\rho_0\alpha + l) = \sqrt{K_z}\rho_0\alpha(1 + k/2) \quad (9.29)$$

2666 With $\nu_z = N\mu_z/2\pi$ and (Eq. 9.15) $K_x = (1 - n)/\rho_0^2$, $K_y = n/\rho_0^2$, $N\alpha = 2\pi$,
 2667 $k = 2l/\rho_0\alpha \ll 1$, this yields for the horizontal and vertical tunes

$$\nu_x \approx \sqrt{1 - n} \left(1 + \frac{k}{2}\right) \approx \sqrt{(1 - n) \frac{R}{\rho_0}}, \quad \nu_y \approx \sqrt{n} \left(1 + \frac{k}{2}\right) \approx \sqrt{n \frac{R}{\rho_0}} \quad (9.30)$$

2668 The identification

$$[T_{\text{per.}}] = I \cos \mu_z + J \sin \mu_z \quad (9.31)$$

2669 allows writing $[T_{\text{per.}}]$ under the form

$$[T_{\text{per.}}] = \begin{bmatrix} \cos \sqrt{K_z}(\rho_0\alpha + l) & \frac{1 + \sqrt{K_z}l \cot(\sqrt{K_z}\rho_0\alpha)}{\sqrt{K_z}} \sin \sqrt{K_z}(\rho_0\alpha + l) \\ -\frac{\sqrt{K_z}}{1 + \sqrt{K_z}l \cot(\sqrt{K_z}\rho_0\alpha)} \sin \sqrt{K_z}(\rho_0\alpha + l) & \cos \sqrt{K_z}(\rho_0\alpha + l) \end{bmatrix} \quad (9.32)$$

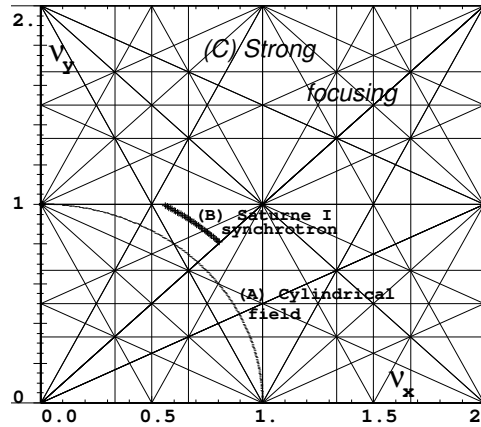
2670 so leading to the optical functions at the center of the drift,

$$\alpha_z = 0, \quad \beta_z = \frac{1}{\sqrt{K_z}} \left[1 + \sqrt{K_z}l \cot(\sqrt{K_z}\rho_0\alpha) \right] \quad (9.33)$$

2671 *Stability diagram*

2672 The “working point” of the synchrotron is the couple (ν_x, ν_y) at which the accel-
 2673 erator is operated, it fully characterizes the focusing. In a structure with cylindrical
 2674 symmetry (cf. Eq. 4.16) $\nu_x = \sqrt{1 - n}$ and $\nu_y = \sqrt{n}$ so that $\nu_x^2 + \nu_y^2 = 1$: when the
 2675 radial field index n is changed the working point stays on a circle of radius 1 in the
 stability diagram (or “tune diagram”, Fig. 9.13). If drift spaces are added, in a first

Fig. 9.13 Location of the working point in the tune diagram, in case of (A) field with revolution symmetry, on a circle of radius 1; (B) sector field with index + drift spaces, on a circle of radius $(\sqrt{R/\rho_0})$; (C) strong focusing, $(|n| \gg 1)$, in large ν_x, ν_y regions.



2676 approximation (Eq. 9.30)
 2677

$$v_x = \sqrt{(1-n)\frac{R}{\rho_0}}, \quad v_y = \sqrt{n\frac{R}{\rho_0}}, \quad v_x^2 + v_y^2 = \frac{R}{\rho_0} \quad (9.34)$$

2678 the working point is located on the circle of radius $\sqrt{R/\rho_0} > 1$.

Horizontal and vertical focusing are not independent: if v_x increases then v_y decreases and reciprocally; none can exceed the limits

$$0 < v_{x,y} < \sqrt{R/\rho_0}$$

2679 This is a lack of flexibility which strong focusing will overcome by providing two
2680 knobs so allowing adjustment of both tunes separately.

2681 Off-momentum orbits

In a dipole with field index $n = -\frac{\rho_0}{B_0} \frac{\partial B_y}{\partial \rho}$, orbits different momenta $p = p_0 + \Delta p$ are concentric (Fig. 9.7), distant (after Eq. 4.18)

$$\Delta x = \frac{\rho_0}{1-n} \frac{\Delta p}{p_0}$$

2682 from the reference orbit. Introduce now the geometrical radius $R = (1+k)\rho_0$ (Eq. 9.7)
2683 to account for the added drifts, this gives

$$\frac{\Delta x}{\Delta p/p_0} \equiv \frac{\Delta R}{\Delta p/p_0} = \frac{R}{(1-n)(1+k)} \quad (9.35)$$

2684 Thus the chromatic dispersion of the orbits, the dispersion function

$$D = \frac{\Delta x}{\Delta p/p_0} = \frac{R}{(1-n)(1+k)}, \quad \text{constant} \quad (9.36)$$

2685 an s -independent quantity: in a structure with axial symmetry, comprising drift
2686 sections (Fig. 9.5) or not (classical and AVF cyclotrons for instance), the ratio
2687 $\frac{\Delta x}{\rho_0 \Delta p/p_0}$ is independent of the azimuth s , the distance of a chromatic orbit to the
2688 reference orbit is constant around the ring.

2689 Given that $n < 1$,

2690 - higher momentum orbits, $p > p_0$, have a greater radius,

2691 - lower momentum orbits, $p < p_0$, have a smaller radius.

2692 Chromatic orbit length

2693 In an axially symmetric structure the difference in closed orbit length $\Delta C = 2\pi\Delta R$
2694 resulting from the difference in momentum arises in the dipoles, as all orbits are
2695 parallel in the drifts (Fig. 9.5). Hence, from Eq. 9.35, the relative closed orbit

2696 lengthening factor, “momentum compaction”

$$\alpha = \frac{\Delta C}{C} \bigg/ \frac{\Delta p}{p_0} \equiv \frac{\Delta R}{R} \bigg/ \frac{\Delta p}{p_0} = \frac{1}{(1-n)(1+k)} \approx \frac{1}{v_x^2} \quad (9.37)$$

2697 with $k = Nl/\pi\rho_0$ (Eq. 9.7). Note that the relationship $\alpha \approx 1/v_x^2$ between momentum
 2698 compaction and horizontal wave number established for a revolution symmetry
 2699 structure (Eq. 4.20) still holds when adding drifts.

2700 **9.1.1.4 Longitudinal Motion**

The acceleration of the ideal particle is addressed in this Section. In a synchrotron,
 the field B is varied (a function performed by the power supply) concurrently with
 the bunch momentum p (a function performed by the accelerating cavity) in such a
 way that at any time

$$B(t)\rho = p(t)/q$$

2701 If this condition is fulfilled, then at all times during the acceleration cycle the central
 2702 trajectory remains on the design optical axis, which is comprised of the reference arc
 2703 in the dipoles, of the axis of the vacuum pipe in the straight section, of the accelerating
 2704 cavities, of the beam position monitors, etc. Given the energies involved, the magnet
 2705 supply imposes its law and the cavity follows $B(t)$, the best in can. A schematic $B(t)$
 law is represented in Fig. 9.14.

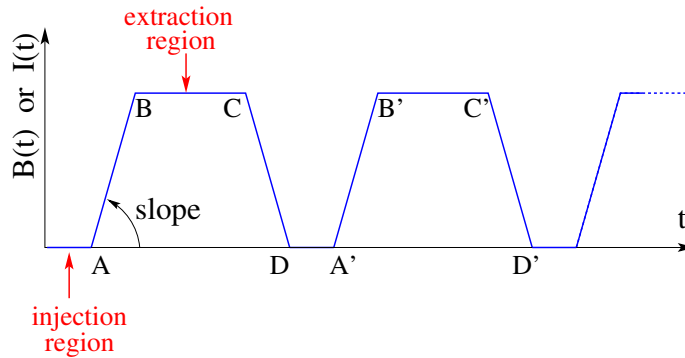


Fig. 9.14 Cycling $B(t)$ in a pulsed synchrotron. Ignoring saturation, $B(t)$ is proportional to the magnet power supply current $I(t)$. Bunch injection occurs at low field, in the region of A, extraction occurs at top energy, on the high field plateau. (AB): field ramp up (acceleration); (BC): flat top (includes beam extraction period); (CD): field ramp down; (DA’): thermal relaxation. (AA’): repetition period; $(1/AA')$: repetition rate; *slope*: ramp velocity $\dot{B} = dB/dt$ (Tesla/s).

2706 Typical values from Saturne I synchrotron are given in Tab. 9.1. As the central trajectory length is fixed ($2\pi R \approx 68.9$ m, see Tab. 9.2) whereas particle velocity

Table 9.1 Saturne I field parameters

\dot{B}	1.8 T/s
B_{\max}	1.5 T
ρ	8.42 m
$B_{\max}\rho$	13 T m

increases turn after turn, thus the revolution time T_{rev} varies.

$$T_{\text{rev}} = \frac{\text{duration of a turn}}{\text{velocity}} = \frac{2\pi R}{\beta c}$$

$$R_{\text{Sat. I}} = 10.97 \text{ m}, \begin{cases} \text{initial E} = 3.6 \text{ MeV} \\ \text{final E} = 2.94 \text{ GeV} \end{cases} \Rightarrow \begin{cases} T_{\text{rev}} = \frac{2\pi R}{0.09 \times 3 \times 10^8} = 16.5 \mu\text{s}; f = 0.06 \text{ MHz} \\ T_{\text{rev}} = \frac{2\pi R}{0.97 \times 3 \times 10^8} = 0.24 \mu\text{s}; f = 4.2 \text{ MHz} \end{cases}$$

The accelerating voltage $\hat{V}(t) = \sin \omega_{\text{rf}} t$ is maintained in synchronism with the revolution motion, thus its angular frequency ω_{rf} follows $h f_{\text{rev}}$,

$$\omega_{\text{rf}} = h \omega_{\text{rev}} = h \frac{c}{R} \frac{B(t)}{\sqrt{\left(\frac{m_0}{q\rho}\right)^2 + B^2(t)}}$$

2707 *Energy gain*

2708 The variation of the particle energy over a turn amounts to the work of the force
2709 $F = dp/dt$ on the charge at the cavity, namely

$$\Delta W = F \times 2\pi R = 2\pi q R \rho \dot{B} \quad (9.38)$$

Over most of the acceleration cycle in a slow-cycling synchrotron \dot{B} is usually constant (Eq. 9.3), thus so is ΔW . At Saturne I for instance

$$\frac{\Delta W}{q} = 2\pi R \rho \dot{B} = 68.9 \times 8.42 \times 1.8 = 1044 \text{ volts}$$

The field ramp lasts

$$\Delta t = (B_{\max} - B_{\min})/\dot{B} \approx B_{\max}/\dot{B} = 0.8 \text{ s}$$

The number of turns to the top energy ($W_{\max} \approx 3 \text{ GeV}$) is

$$N = \frac{W_{\max}}{\Delta W} = \frac{3 \times 10^9 \text{ eV}}{1044 \text{ eV}} \approx 3 \times 10^6$$

2710 *Adiabatic damping of the betatron oscillations*

During acceleration, focusing strengths follow the increase of particle rigidity, so to maintain the tunes ν_x and ν_y constant. As a result of the longitudinal acceleration at the cavity though, the longitudinal energy of the particles is modified. This results in a decrease of the amplitude of betatron oscillations (an increase if the cavity is decelerating). The mechanism is sketched in Fig. 9.15: the slope, respectively before (index 1) and after (index 2) the cavity is

$$\frac{dx}{ds} = \frac{m \frac{dx}{dt}}{m \frac{ds}{dt}} = \frac{p_x}{p_s}, \quad \frac{dx}{ds} \Big|_2 = \frac{m \frac{dx}{dt}}{m \frac{ds}{dt}} \Big|_2 = \frac{p_{x,2}}{p_{s,2}}$$

Particle mass and velocity are modified at the traversal of the cavity but, as the

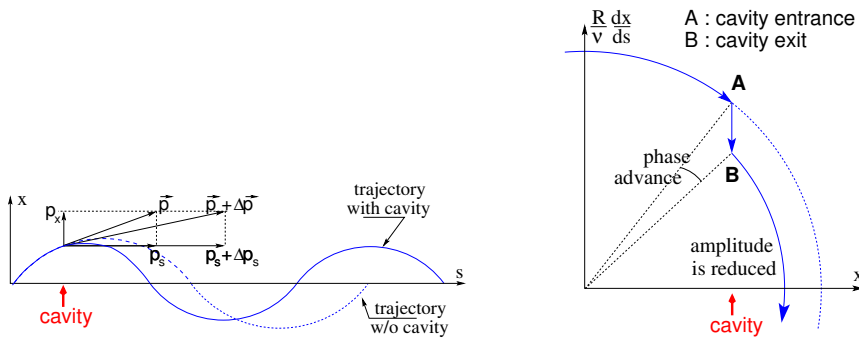


Fig. 9.15 Adiabatic damping of betatron oscillations, here from $x' = p_x/p_s$ before the cavity, to $x'_2 = p_x/(p_s + \Delta p_s)$ after the cavity. In the horizontal phase space, to the right, decrease of $\Delta \left(\frac{dx}{ds} \right)$ if $\frac{dx}{ds} > 0$, increase of $\Delta \left(\frac{dx}{ds} \right)$ if $\frac{dx}{ds} < 0$

force is longitudinal, $dp_x/dt = 0$ thus $p'_x = p_x$, the increase in momentum is purely longitudinal, $p'_s = p_s + \Delta p$. Thus

$$\frac{dx}{ds} \Big|_2 = \frac{p_x}{p_s + \Delta p} \approx \frac{p_x}{p_s} \left(1 - \frac{\Delta p}{p_s} \right)$$

and as a consequence the slope dx/ds varies across the cavity,

$$\Delta \left(\frac{dx}{ds} \right) = \frac{dx}{ds} \Big|_2 - \frac{dx}{ds} = - \frac{dx}{ds} \frac{\Delta p_s}{p_s}$$

- 2711 The slope varies in proportion to the slope, with opposite sign if $\Delta p/p > 0$ (acceleration) thus a decrease of the slope. This variation has two consequences on the
- 2712 betatron oscillation (Fig. 9.15):
- 2713 - a change of the betatron phase,
- 2714 - a modification of the betatron amplitude.
- 2715

2716 *In matrix form*

2717 Coordinate transport through the cavity writes $\begin{cases} x_2 = x \\ x_2' \approx \frac{p_x}{p_s} (1 - \frac{dp}{p}) = x' (1 - \frac{dp}{p}) \end{cases}$,
 2718 hence the transfer matrix of the cavity,

$$[C] = \begin{bmatrix} 1 & 0 \\ 0 & 1 - \frac{dp}{p} \end{bmatrix} \quad (9.39)$$

2719 its determinant is $1 - dp/p \neq 1$: the system is non-conservative (the surface in phase
 2720 space is not conserved). Assume one cavity in the ring and not $[T] \times [C]$ the one-turn
 2721 matrix with origin at entrance of the cavity. Its determinant is $\det[T] \times \det[C] =$
 2722 $\det[C] = 1 - \frac{dp}{p}$. Over N turns the coordinate transport matrix is $([T][C])^N$, its
 2723 determinant is $(1 - \frac{dp}{p})^N \approx 1 - N \frac{dp}{p}$. The surface of the longitudinal beam ellipse
 2724 is $\varepsilon_l \times \det[T]_{turn} = \varepsilon_{l,0} - \varepsilon_l \frac{dp}{p}$ thus $\frac{d\varepsilon_l}{\varepsilon_l} = -\frac{dp}{p}$, the solution of which is

$$\varepsilon_l \times p = constant, \text{ or } \beta\gamma\varepsilon = constant \quad (9.40)$$

2725 *Synchrotron motion; the synchronous particle*

2726 By “synchrotron motion”, or “phase oscillations”, it is meant a mechanism that
 2727 stabilizes the longitudinal motion of a particle around a synchronous phase, in virtue
 2728 of

2729 (i) the presence of an accelerating cavity with its frequency indexed on the
 2730 revolution time,

2731 (ii) with the bunch centroid positioned either on the rising slope of the oscillating
 2732 voltage (low energy regime), or on the falling slope (high energy regime).

The synchronous (or “ideal”) particle follows the equilibrium trajectory around
 the ring (the reference closed orbit, about which all other particles will undergo a
 betatron oscillation) and its velocity satisfies

$$B\rho = \frac{p}{q} = \frac{mv}{p} \rightarrow v = \frac{qB\rho}{m}$$

2733 - the revolution time is $T_{rev} = \frac{2\pi R}{v} = \frac{2\pi R}{\beta c} = \frac{2\pi R}{qB\rho/m}$
 - the angular revolution frequency follows the increase of B:

$$\omega_{rev} = \frac{2\pi}{T_{rev}} = \frac{qB\rho}{mR}$$

2734 - during the acceleration $B(t)$ increases at a $\frac{dB}{dt} = \dot{B}$ rate normally of the order of a
 2735 Tesla/second.

- in order for the ideal particle to stay on the closed orbit during the acceleration, its
 changing momentum must at all time satisfy $B(t)\rho = p(t)/q$. This defines $p(t)$ as a

function of $B(t)$, and the following B dependence of mass and angular frequency:

$$m(t) = \gamma(t)m_0 = \frac{q\rho}{c} \sqrt{\left(\frac{m_0}{qc\rho}\right)^2 + B(t)^2}$$

$$\omega_{rev}(t) = \frac{c}{R} \frac{B(t)}{\sqrt{\left(\frac{m_0}{qc\rho}\right)^2 + B(t)^2}}$$

2736 - the RF voltage frequency $\omega_{RF}(t) = h\omega_{rev}(t)$ follows $B(t)$, this maintains the
2737 synchronous phase at a fixed value

2738 - over a turn the gain in energy is $\Delta W = 2\pi qR\rho\dot{B}$, the reference particle experiences
2739 a voltage $V = \Delta W/q = 2\pi R\rho\dot{B}$.

2740 Simulation wise, the ramping of the guide field can be assumed to follow a step
2741 function in correlation with the step increase of particle momentum at the RF cavity.
2742 In that manner, the synchronous particle is maintained on the design orbit, at radius
2743 $\rho = p(t)/qB(t) = \text{constant}$ in the guide magnets.

2744 *Phase Stability*

2745 The mechanism of phase stability has, first experimented in the synchrocyclotron [14]
2746 has been introduced in the eponym Chapter (Chap. 8). It is re-visited here accounting
2747 for specificities of the operation of a synchrotron, such as the constant radius orbit,
2748 or the concept of transition energy.

Note ϕ_s the RF phase at arrival of the synchronous particle at the aforementioned
accelerating cavity, its energy gain is

$$\Delta W = q\hat{V} \sin \phi_s = 2\pi qR\rho\dot{B}$$

The condition $|\sin \phi_s| < 1$ imposes a lower limit to the cavity voltage for acceleration
to happen, namely

$$\hat{V} > 2\pi R\rho\dot{B}$$

2749 Referring to Fig. 9.16, the synchronous phase can be placed on the left (A A' A''...
2750 series in the Figure, or on the right (B B' B''... series) of the oscillating voltage crest.
2751 One and only one of these two possibilities, and which one depends on the optical
2752 lattice and on particle energy, ensures that particles in a bunch remain grouped in the
2753 vicinity of the synchronous particles. The transition between these two regimes (A
2754 series or B series) occurs at the transition γ , γ_{tr} , a property of the lattice. If the bunch
2755 energy is below transition energy, $E_{\text{bunch}} < m\gamma_{tr}$, the bunch has to present itself on
2756 the left of the crest (A series), if the bunch energy is greater than transition energy,
2757 $E_{\text{bunch}} > m\gamma_{tr}$, the bunch has to present itself on the right of the crest (B series).

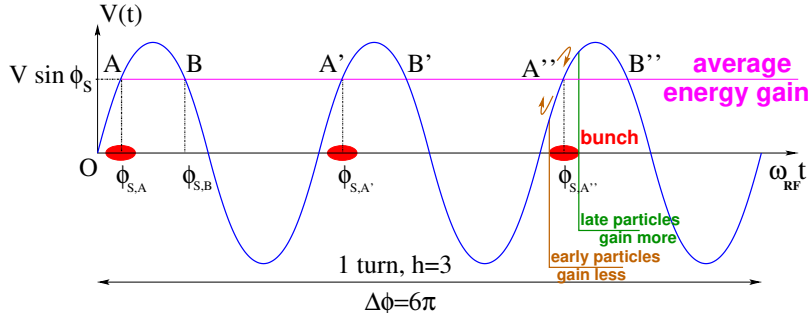


Fig. 9.16 Mechanism of phase stability, “longitudinal focusing”. Below transition ($\gamma < \gamma_{tr}$) phase stability occurs for a synchronous phase taken at either of the $h=3$ stable locations A, A', A'': a particle with higher energy goes around the ring more rapidly than the synchronous particle, it arrives earlier at the voltage gap (at $\phi < \phi_{s,A}$) and experiences a lower voltage; at lower energy the particle is slower, it arrives at the gap later compared to the synchronous particle, at $\phi > \phi_{s,A}$, and experiences a greater voltage; this results overall in a stable oscillatory motion around the synchronous phase. Beyond transition ($\gamma > \gamma_{tr}$) the stable phase is at either of the $h=3$ stable locations B, B', B'': a particle which is less energetic than the synchronous particle arrives earlier, $\phi < \phi_{s,B}$, it experiences a greater voltage, and inversely when it eventually gets more energetic than the synchronous particle

2758 *Transition energy*

2759 The transition between the two regimes occurs at $\frac{dT_{rev}}{T_{rev}} = 0$. With $T = 2\pi/\omega = C/v$,
 2760 this can be written $\frac{d\omega_{rev}}{\omega_{rev}} = -\frac{dT_{rev}}{T_{rev}} = \frac{dv}{v} - \frac{dC}{C}$. With $\frac{dv}{v} = \frac{1}{\gamma^2} \frac{dp}{p}$ and momentum
 2761 compaction $\alpha = \frac{dC}{C} / \frac{dp}{p}$, (Eq. 9.37), this can be written

$$\frac{d\omega_{rev}}{\omega_{rev}} = -\frac{dT_{rev}}{T_{rev}} = \left(\frac{1}{\gamma^2} - \alpha\right) \frac{dp}{p} = \eta \frac{dp}{p} \quad (9.41)$$

2762 wherein the phase-slip factor has been introduced,

$$\eta = \overbrace{\frac{1}{\gamma^2}}^{\text{kinematics}} - \underbrace{\alpha}_{\text{lattice}} \quad (9.42)$$

2763 In a weak focusing structure $\alpha \approx 1/v_x^2$ (Eqs. 4.20, 9.37), thus the phase stability
 2764 regime is

$$\text{below transition, i.e. } \phi_s < \pi/2, \quad \text{if } \gamma < v_x \quad (9.43)$$

$$\text{above transition, i.e. } \phi_s > \pi/2, \quad \text{if } \gamma > v_x \quad (9.44)$$

$$(9.45)$$

2765 In weak focusing synchrotrons the horizontal tune $\nu_x = \sqrt{(1-n)R/\rho_0}$ (Eq. 9.30)
 2766 may be ≥ 1 , and subsequently $\gamma_{tr} \approx \nu_x \geq 1$ depending on the horizontal tune value.
 2767 Saturne I for instance, with $\nu_x \approx 0.7$ (Tab. 9.2), operated above transition energy.

2768 9.1.2 Spin Motion, Depolarizing Resonances

2769 The availability of polarized proton sources allowed the acceleration of polarized
 2770 beams to high energy. The possibility was considered from the early times of the
 2771 ZGS [15], up to 70% polarization transmission through the synchrotron was fore-
 2772 seen, polarization manipulation concepts included harmonic orbit correction, tune
 2773 jump at strongest depolarizing resonances (Fig. 9.17). Acceleration of a polarized
 2774 proton beam happened for the first time in a synchrotron and to multi-GeV energy in
 2775 1973, four years after the ZGS startup. Beams were accelerated up to 17 GeV with
 2776 substantial polarization maintained [8]. Experiments were performed to assess the
 2777 possibility of polarization transmission in strong focusing synchrotrons, and polar-
 2778 ization lifetime in colliders [16]. Acceleration of polarized deuteron was achieved in
 2779 the late 1970s, when sources were made available [17].

2780 The field index is essentially zero in the ZGS, transverse focusing is ensured
 2781 by wedge angles at the ends of the height dipoles, which is thus the only location
 2782 where non-zero horizontal field components are found. The vertical wave number
 2783 is small in addition, less than 1. This results in depolarizing resonance strengths
 2784 on the weak side, “As we can see from the table, the transition probability [from
 2785 spin state $\psi_{1/2}$ to spin state $\psi_{-1/2}$] is reasonably small up to $\gamma = 7.1$ ” [8], i.e.
 2786 $G\gamma = 12.73$, $p = 6.6$ GeV/c; the table referred to stipulates a transition probability
 2787 $P_{\frac{1}{2}, -\frac{1}{2}} < 0.042$, whereas resonances beyond that energy range feature $P_{\frac{1}{2}, -\frac{1}{2}} > 0.36$.
 2788 Beam depolarization up to 6 GeV/c, under the effect of these resonances, is illustrated
 2789 in Fig. 9.17.

2790 In weak focusing synchrotron particles experience radial fields all along the
 2791 bend dipoles as an effect of the radial field index, as they undergo vertical betatron
 2792 oscillations. However these radial field components are weak, and so is there effect
 2793 on spin motion, as long as the particle energy (the γ factor in the spin precession
 2794 equation) is not too high.

Assuming a defect-free ring, the vertical betatron motion excites “intrinsic” spin resonances, located at

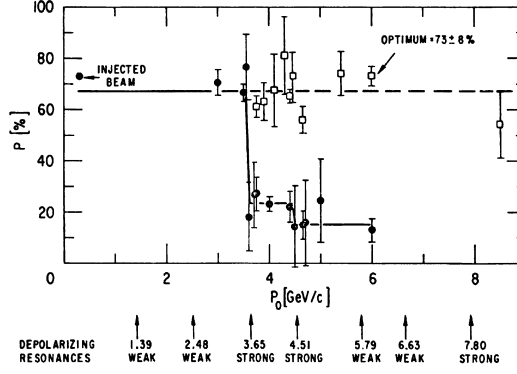
$$G\gamma_R = kP \pm \nu_y$$

with k an integer and P the period of the ring. In the ZGS for instance, $\nu_y \approx 0.8$
 (Tab. 9.3), the ring $P=4$ -periodic, thus $G\gamma_R = 4k \pm 0.8$. Strongest resonances are
 located at

$$G\gamma_R = MPk \pm \nu_y$$

2795 with M the number of cells per superperiod [18, Sec. 3.II]. In the ZGS, $M=2$ thus
 2796 strongest resonances occur at $G\gamma_R = 2 \times 4k \pm 0.8$.

Fig. 9.17 Depolarizing intrinsic resonance landscape up to 6 GeV/c at the ZGS (solid circles). Systematic resonances are located at $G\gamma_R = 4 \times \text{integer} \pm \nu_y$, stronger ones at $G\gamma_R = 8 \times \text{integer} \pm \nu_y$. Tune jump was used to preserve polarization when crossing strong resonances (empty circles) [?]



In the presence of vertical orbit defects, non-zero periodic transverse fields are experienced along the closed orbit, they excite “imperfection” depolarizing resonances, located at

$$G\gamma_R = k$$

with k an integer. In the case of systematic defects the periodicity of the orbit is that of the lattice, P , imperfection resonances are located at $G\gamma_R = kP$. Strongest imperfection resonances are located at

$$G\gamma_R = MPk$$

2797 with M the number of cells per superperiod [18, Sec. 3.II]. Crossing a depolarizing
2798 resonance, during acceleration, causes a loss of polarization given by (Froissart-Stora
2799 formula [19])

$$\frac{P_f}{P_i} = 2e^{-\frac{\pi}{2} \frac{|\epsilon_R|^2}{\alpha}} - 1 \quad (9.46)$$

2800 from a value P_i upstream to an asymptotic value P_f downstream of the resonance.
2801 This assumes an isolated resonance, passed with a crossing speed

$$\alpha = G \frac{d\gamma}{d\theta} = \frac{1}{2\pi} \frac{\Delta E}{M} \quad (9.47)$$

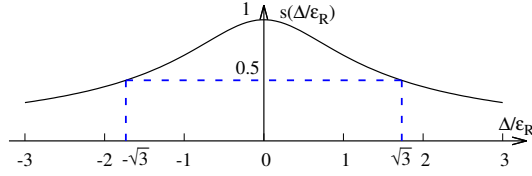
2802 with ΔE the energy gain per turn and M the mass. ϵ_R is the resonance strength.

2803 *Spin precession axis. Resonance width*

2804 Consider the spin vector $\mathbf{S}(\theta) = (S_\eta, S_\xi, S_y)$ of a particle in the laboratory frame,
2805 with θ the orbital angle around the accelerator. Introduce the projection $s(\theta)$ of \mathbf{S}
2806 in the median plane

$$s(\theta) = S_\eta(\theta) + jS_\xi(\theta) \quad (\text{and } S_y^2 = 1 - s^2) \quad (9.48)$$

Fig. 9.18 Modulus of the horizontal spin component. $s = 1/2$ at distance $\Delta = \pm\sqrt{3}\epsilon_R$ from $G\gamma_R$



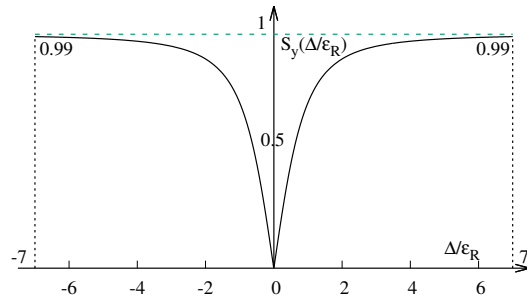
2807
2808
2809

It can be shown that in the case of a stationary solution of the spin motion (*i.e.*, the spin precession axis) s satisfies [20] (Fig. 9.18)

$$s^2 = \frac{1}{1 + \frac{\Delta^2}{|\epsilon_R|^2}} \quad (9.49)$$

wherein $\Delta = G\gamma - G\gamma_R$ is the distance to the resonance. The resonance width is a

Fig. 9.19 Dependence of polarization on the distance to the resonance. For instance $S_y = 0.99$, 1% depolarization, corresponds to $\Delta = 7|\epsilon_R|$. On the resonance, $\Delta = 0$, the precession axis lies in the median plane, $S_y = 0$



2810
2811
2812

measure of its strength (Fig. 9.19). The quantity of interest is the angle, ϕ , of the spin precession direction to the vertical axis, given by (Fig. 9.19)

$$\cos \phi(\Delta) \equiv S_y(\Delta) = \sqrt{1 - s^2} = \frac{\Delta/|\epsilon_R|}{\sqrt{1 + \Delta^2/|\epsilon_R|^2}} \quad (9.50)$$

2813
2814
2815
2816

On the resonance, $\Delta = 0$, the spin precession axis lies in the bend plane: $\phi = \pm\pi/2$. $S_y = 0.99$ (1% depolarization) corresponds to a distance to the resonance $\Delta = 7|\epsilon_R|$, and spin precession axis at an angle $\phi = \arccos(0.99) = 8^\circ$ from the vertical.

Conversely,

$$\frac{\Delta^2}{|\epsilon_R|^2} = \frac{S_y^2}{1 - S_y^2} \quad (9.51)$$

The precession axis is common to all spins, S_y is a measure of the polarization along the vertical axis,

$$S_y = \frac{N^+ - N^-}{N^+ + N^-}$$

2817 wherein N^+ and N^- denote the number of particles in spin states $\frac{1}{2}$ and $-\frac{1}{2}$ respec-
2818 tively.

2819 *Spin motion through weak resonances*

Depolarizing resonances are weak up to several GeV in a weak focusing synchrotron, as the radial and/or longitudinal fields, which stem from a small radial field index and from dipole fringe fields, are weak. Spin motion $S_y(\theta)$ through a resonance in that case (*i.e.*, assuming $S_{y,f} \approx S_{y,i}$, with $S_{y,f}$ and $S_{y,i}$ the asymptotic vertical spin component values respectively upstream and downstream of the resonance) can be calculated in terms of the Fresnel integrals

$$C(x) = \int_0^x \cos\left(\frac{\pi}{2}t^2\right) dt, \quad S(x) = \int_0^x \sin\left(\frac{\pi}{2}t^2\right) dt$$

namely, with the origin of the orbital angle taken at the resonance [20] (Fig. 9.20)

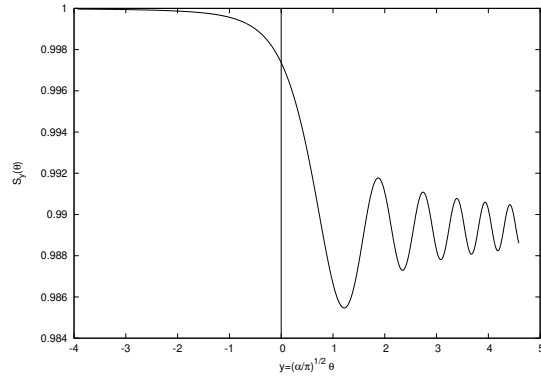


Fig. 9.20 Vertical component of spin motion $S_y(\theta)$ through a weak depolarizing resonance (after Eq. 9.52). The vertical bar is at the location of the resonance, which coincides with the origin of the orbital angle

2820

$$\begin{aligned} \text{if } \theta < 0 : \left(\frac{S_y(\theta)}{S_{y,i}} \right)^2 &= 1 - \frac{\pi}{\alpha} |\epsilon_R|^2 \left\{ \left[0.5 - C\left(-\theta\sqrt{\frac{\alpha}{\pi}}\right) \right]^2 + \left[0.5 - S\left(-\theta\sqrt{\frac{\alpha}{\pi}}\right) \right]^2 \right\} \\ \text{if } \theta > 0 : \left(\frac{S_y(\theta)}{S_{y,i}} \right)^2 &= 1 - \frac{\pi}{\alpha} |\epsilon_R|^2 \left\{ \left[0.5 + C\left(\theta\sqrt{\frac{\alpha}{\pi}}\right) \right]^2 + \left[0.5 + S\left(\theta\sqrt{\frac{\alpha}{\pi}}\right) \right]^2 \right\} \end{aligned} \quad (9.52)$$

2821 In the asymptotic limit,

$$\frac{S_y(\theta)}{S_{y,i}} \xrightarrow{\theta \rightarrow \infty} 1 - \frac{\pi}{\alpha} |\epsilon_R|^2 \quad (9.53)$$

2822 which identifies with the development of Froissart-Stora formula $P_f/P_i = 2 \exp(-\frac{\pi}{2} \frac{|\epsilon_R|^2}{\alpha}) -$
2823 1, to first order in $|\epsilon_R|^2/\alpha$. This approximation holds in the limit that higher order
2824 terms can be neglected, viz. $|\epsilon_R|^2/\alpha \ll 1$.

2825 9.2 Exercises

2826 9.1 Construct Saturne I synchrotron. Spin Resonances

2827 Solution: page 348

2828 In this exercise, Saturne I synchrotron is modeled in `zgoubi`, and spin resonances
2829 in a weak focusing gradient synchrotron are studied.

2830 (a) Construct a model of Saturne I 90° cell dipole in the hard-edge model, using
2831 DIPOLE. Use parameters given in Tab. 9.2, and Fig. 9.21 as a guidance. It is judicious
2832 (although in no way a necessity) to take $RM=841.93$ cm in DIPOLE.

2833 Provide the 6×6 transport matrix of that dipole. MATRIX can be used for that,
2834 with OBJET[KOBJ=5] to define a proper set of initial coordinates.

2835 Check against theory (refer to Sect. 18.2, Eq. 18.31).

2836 (b) Construct a model of Saturne I four-cell synchrotron. Assume that the reference
2837 orbit has the nominal radius in the dipoles, 841.93 cm.

2838 Compute the tunes using MATRIX; check their values against theory.

2839 Produce a scan of the tunes over the field index range $0.5 \leq n \leq 0.757$. RE-
2840 BELOTE can be used to repeatedly change n over that range. Superimpose the
2841 theoretical curves $\nu_x(n)$, $\nu_y(n)$.

2842 Using TWISS and OBJET[KOBJ=5], produce the periodic beam matrix of the
2843 ring. TWISS causes a print out of both the transport matrix and the periodic beam
2844 matrix: check that these satisfy Eq. 9.31.

2845 (c) Launch 50 particles evenly distributed on a common paraxial horizontal
2846 Courant-Snyder invariant (vertical motion is taken null). Store particle data along
2847 the ring in `zgoubi.plt`, using DIPOLE[IL=2] and DRIFT[split,N=20,IL=2]. Use these
2848 to produce a graph of $x^2(s) / \epsilon_x / \pi$.

2849 From this graph, get the value of the betatron function β_x at the ends of the cell,
2850 compare with TWISS outcomes. Find the minimum and maximum values of the
2851 beta functions, and their azimuth $s(\min[\beta_x])$, $s(\max[\beta_x])$. Check the latter against
2852 theory.

2853 Repeat for the vertical motion, taking $\epsilon_x = 0$, ϵ_y paraxial.

2854 (d) Answer the previous question using, instead of 50 particles, a single particle
2855 traced over 50 turns.

2856 (e) Find the closed orbit for an off-momentum particle. FIT can be used for that.
2857 From the raytracing outcome, produce a graph of the dispersion function $D_x(s)$ so
2858 obtained.

(f) Justify considering the betatron oscillation as sinusoidal, namely,

$$y(\theta) = A \cos(\nu_y \theta + \phi)$$

2859 wherein $\theta = s/R$, $R = \oint ds / 2\pi$.

2860 Find the value of the horizontal and vertical betatron functions, resulting from
2861 that approximation. Compare with the betatron functions obtained in (b).

2862 (g) Produce an acceleration cycle from 3.6 MeV to 3 GeV, for a few particles
2863 launched on a common $10^{-4} \pi m$ initial invariant in each plane. Ignore synchrotron
2864 motion (CAVITE[IOPT=3] can be used in that case). Take a peak voltage $\hat{V} = 200$ kV

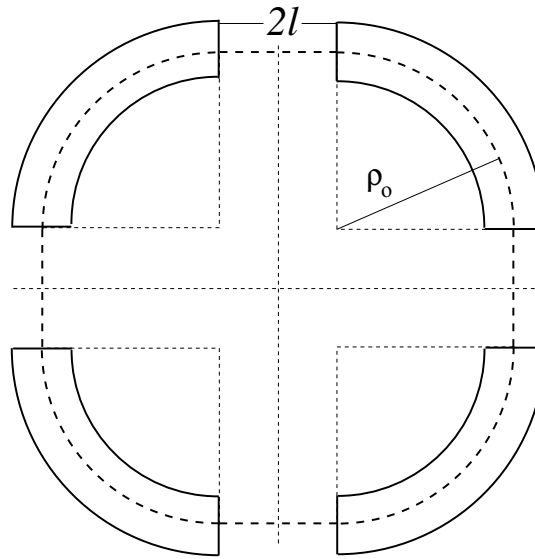


Fig. 9.21 A schematic layout of Saturne I, a $2\pi/4$ axial symmetry structure, comprised of 4 radial field index 90 deg dipoles and 4 drift spaces. The cell in the simulation exercises is taken as a $\pi/4$ quadrant: l-drift/90°-dipole/l-drift

Table 9.2 Parameters of Saturne 1 weak focusing synchrotron [21]. ρ_0 denotes the reference bending radius in the dipole; the reference orbit, field index, wave numbers, etc., are taken along that radius

Orbit length, C	cm	6890
Equivalent radius, R	cm	1096.58
Straight section length, $2l$	cm	400
Magnetic radius, ρ_0	cm	841.93
R/ρ_0		1.30246
Field index n , nominal value		0.6
Wave numbers, $\nu_x; \nu_y$		0.724; 0.889
Stability limit		$0.5 < n < 0.757$
Injection energy	MeV	3.6
Field at injection	kG	0.0326
Top energy	GeV	2.94
Field at top energy	kG	14.9
Field ramp at injection	kG/s	20
Synchronous energy gain	keV/turn	1.160
RF harmonic		2

2865 (unrealistic though, as it would result in a nonphysical \dot{B} (Eq. 9.38)) and synchronous
 2866 phase $\phi_s = 150$ deg (justify $\phi_s > \pi/2$).

2867 Check the accuracy of the betatron damping over the acceleration range, compared
 2868 to theory.

2869 How close to symplectic the numerical integration is (it is by definition *not*
 2870 symplectic, being a truncated Taylor series method [22, Eq. 1.2.4]), depends on the
 2871 integration step size, and on the size of the flying mesh in the DIPOLE method [22,
 2872 Fig. 20]; check a possible departure of the betatron damping from theory as a function
 2873 of these parameters.

2874 Produce a graph of the the evolution of the horizontal and vertical wave numbers
2875 during the acceleration cycle.

2876 (h) Change the peak voltage to $\hat{V} = 20$ kV. Produce a graph of the value of the
2877 vertical spin component of the particles as a function of $G\gamma$, over the acceleration
2878 range from 3.6 MeV to 3 GeV. Adding SPNTRK will ensure spin tracking.

2879 Produce a graph of the average value of S_Z over that 200 particle set, as a function
2880 of $G\gamma$. Indicate on that graph the location of the resonant $G\gamma_R$ values.

2881 (i) Based on the simulation file used in (f), simulate the acceleration of a single
2882 particle, through the intrinsic resonance $G\gamma_R = 4 - \nu_Z$, from a few thousand turns
2883 upstream to a few thousand turns downstream.

2884 Perform this resonance crossing for five different values of the particle invariant,
2885 namely: $\varepsilon_Z/\pi = 2, 10, 20, 40, 200 \mu\text{m}$.

2886 Compute P_f/P_i in each case, check the dependence on ε_Z against theory. Com-
2887 pute the resonance strength in each case, check the dependence on ε_Z against theory.

2888 Re-do this crossing simulation for a different crossing speed (take for instance
2889 $\hat{V} = 10$ kV) and a couple of vertical invariant values, compute P_f/P_i so obtained.
2890 Check the crossing speed dependence of P_f/P_i against theory.

2891 (j) Plot the turn-by-turn vertical spin component motion $S_Z(\text{turn})$ across the
2892 resonance $G\gamma_R = 4 - \nu_Z$, in a weakly depolarizing case, $P_f \approx P_i$. Show that it
2893 satisfies Eq. 9.52. Match the data to the latter to get the vertical betatron tune ν_y , and
2894 the location of the resonance $G\gamma_R$.

2895 (k) Track a few particles at fixed energy, at distances from the resonance $G\gamma_R =$
2896 $4 - \nu_y$ of up to a $7 \times \varepsilon_R$ (this distance corresponds to 1% depolarization).

2897 Produce on a common graph the spin motion $S_Z(\text{turn})$ for all these particles, as
2898 observed at some azimuth along the ring.

2899 Produce a graph of $\langle S_y \rangle|_{\text{turn}}(\Delta)$ (as in Fig. 9.19).

Produce the vertical betatron tune ν_y , and the location of the resonance $G\gamma_R$,
obtained from a match of these tracking trials to the theoretical (Eq. 9.50)

$$\langle S_y \rangle (\Delta) = \frac{\Delta}{\sqrt{|\varepsilon_R|^2 + \Delta^2}}$$

2900 9.2 Construct the ZGS synchrotron. Spin Resonances

2901 Solution: page 377

2902 In this exercise, ZGS synchrotron is modeled in zgoubi, and spin resonances in
2903 this weak focusing zero-gradient synchrotron are studied.

2904 (a) Construct an approximate model of the ZGS synchrotron, using DIPOLE.
2905 Use Figs. 9.22, 9.23 as a guidance, and parameters given in Tab. 9.3. Assume that
2906 the reference orbit is the same at all energies, on nominal radius, 2076 cm. It is
2907 judicious (although in no way an obligation) to take RM=2076 in DIPOLE. (Note
2908 that in reality, unlike the present assumption for this exercise, the reference orbit in
2909 ZGS would be moved outward during acceleration [23].)

2910 Check the correctness of the model by producing the lattice parameters of the
2911 ring. TWISS can be used for that. Compare with the lattice parameters given in
2912 Tab. 9.3.

2913 (b) Produce a graph of the betatron functions along the ZGS cell. Provide checks
 2914 of the correctness of the computation.

2915 Check the theoretical periodic dispersion (Eq. 9.36) against the radial distance
 2916 between on- and off-momentum closed orbits obtained from raytracing. Provide a
 2917 plot of the dispersion function.

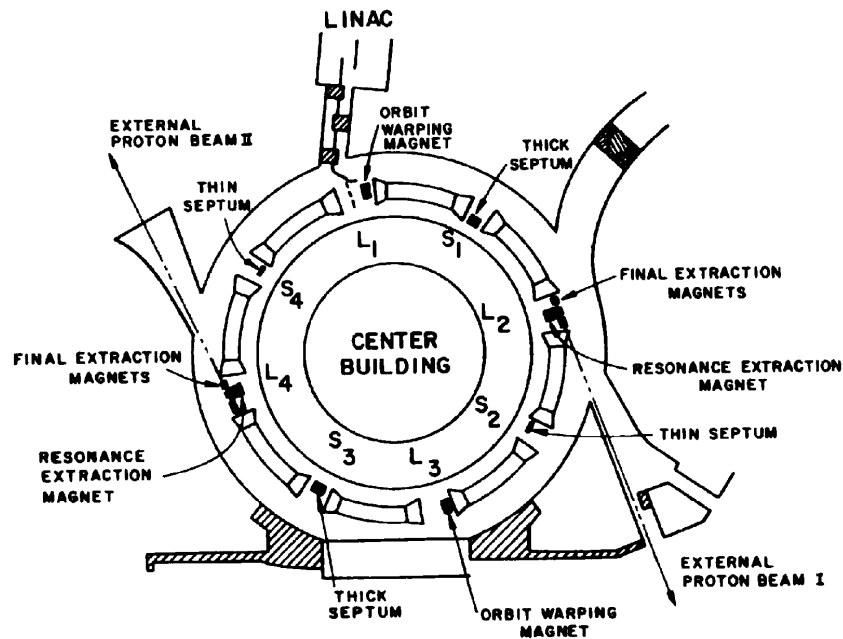


Fig. 9.22 A schematic layout of the ZGS [?], a $\pi/2$ -periodic structure, comprised of 8 zero-index dipoles, 4 long and 4 short straight sections

2918 (c) Additional verifications regarding the model.
 2919 Produce a graph of the field $B(s)$
 2920 - along the on-momentum closed orbit, and along off-momentum chromatic closed
 2921 orbits, across a cell;
 2922 - along orbits at large horizontal excursion;
 2923 - along orbits at large vertical excursion.
 2924 For all these cases, verify qualitatively, from the graphs, that $B(s)$ appears as
 2925 expected.

(d) Justify considering the betatron oscillation as sinusoidal, namely,

$$y(\theta) = A \cos(\nu_y \theta + \phi)$$

2926 wherein $\theta = s/R$, $R = \oint ds/2\pi$.

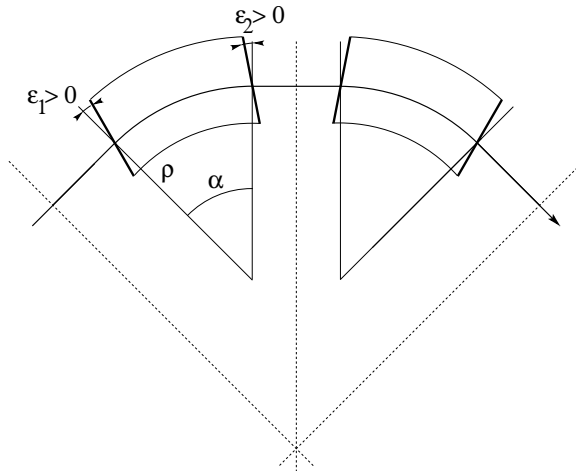


Fig. 9.23 A sketch of ZGS cell layout. In defining the entrance and exit faces (EFBs) of the magnet, beam goes from left to right. Wedge angles at the long straight sections (ϵ_1) and at the short straight sections (ϵ_2) are different

2927 Find the value of the horizontal and vertical betatron functions, resulting from
2928 that approximation. Compare with the betatron functions obtained in (b).

2929 (e) Produce an acceleration cycle from 50 MeV to 17 GeV about, for a few particles
2930 launched on the a common $10^{-5} \pi$ m vertical initial invariant, with small horizontal
2931 invariant. Ignore synchrotron motion (CAVITE[IOPT=3] can be used in that case).
2932 Take a peak voltage $\hat{V} = 200$ kV (this is unrealistic but yields 10 times faster
2933 computing than the actual $\hat{V} = 20$ kV, Tab. 9.3) and synchronous phase $\phi_s = 150$ deg
2934 (justify $\phi_s > \pi/2$). Add spin, using SPNTRK, in view of the next question, (f).

2935 Check the accuracy of the betatron damping over the acceleration range, compared
2936 to theory. How close to symplectic the numerical integration is (it is by definition
2937 *not* symplectic), depends on the integration step size, and on the size of the flying
2938 mesh in the DIPOLE method [22, Fig. 20]; check a possible departure of the betatron
2939 damping from theory as a function of these parameters.

2940 Produce a graph of the the evolution of the horizontal and vertical wave numbers
2941 during the acceleration cycle.

2942 (f) Using the raytracing material developed in (e): produce a graph of the vertical
2943 spin component of the particles, and the average value over that 200 particle set, as
2944 a function of $G\gamma$. Indicate on that graph the location of the resonant $G\gamma_R$ values.

Table 9.3 Parameters of the ZGS weak focusing synchrotron after Refs. [23, 24] [?, pp.288-294,p.716] (2nd column, when they are known) and in the present simplified model and numerical simulations (3rd column). Note that the actual orbit is skewed (moves) during ZGS acceleration cycle, tunes change as well - this is not the case in the present modeling

		From Refs. [23, 24]	Simplified model
Injection energy	MeV		50
Top energy	GeV		12.5
$G\gamma$ span		1.888387 - 25.67781	
Length of central orbit	m	171.8	170.90457
Length of straight sections, total	m	41.45	40.44
<i>Lattice</i>			
Wave numbers $\nu_x; \nu_y$		0.82; 0.79	0.849; 0.771
Max. $\beta_x; \beta_y$	m		32.5; 37.1
<i>Magnet</i>			
Length	m	16.3	16.30486 (magnetic)
Magnetic radius	m	21.716	20.76
Field min.; max.	kG	0.482; 21.5	0.4986; 21.54
Field index			0
Yoke angular extent	deg	43.02590	45
Wedge angle	deg	≈ 10	13 and 8
<i>RF</i>			
Rev. frequency	MHz	0.55 - 1.75	0.551 - 1.751
RF harmonic $h = \omega_{rf} / \omega_{rev}$			8
Peak voltage	kV	20	200
B-dot, nominal/max.	T/s	2.15/2.6	
Energy gain, nominal/max.	keV/turn	8.3/10	100
Synchronous phase, nominal	deg		150
<i>Beam</i>			
$\varepsilon_x; \varepsilon_y$ (at injection)	$\pi \mu\text{m}$		25; 150
Momentum spread, rms			3×10^{-4}
Polarization at injection	%	>75	100
Radial width of beam (90%), at inj.	inch	2.5	$\sqrt{\beta_x \varepsilon_x / \pi} = 1.1$

2945 (g) Based on the simulation file used in (f), simulate the acceleration of a single
 2946 particle, through one particular intrinsic resonance, from a few thousand turns
 2947 upstream to a few thousand turns downstream.

2948 Perform this resonance crossing for different values of the particle invariant.
 2949 Determine the dependence of final/initial vertical spin component value, on the
 2950 invariant value; check against theory.

2951 Re-do this crossing simulation for a different crossing speed. Check the crossing
 2952 speed dependence of final/initial vertical spin component so obtained, against theory.

2953 (h) Introduce a vertical orbit defect in the ZGS ring.

2954 Find the closed orbit.

2955 Accelerate a particle launched on that closed orbit, from 50 MeV to 17 GeV about,
 2956 produce a graph of the vertical spin component.

2957 Select one particular resonance, reproduce the two methods of (g) to check the
 2958 location of the resonance at $G\gamma_R = \text{integer}$, and to find its strength.

2959 References

- 2960 1. Veksler, V.: A new method of acceleration of relativistic particles. J. of Phys. USSR 9 153-158
 2961 (1945)
- 2962 2. McMillan, E. M.: The Synchrotron. Phys. Rev. 68 143-144 (1945)
- 2963 3. Goward, F. K., and Barnes, D. E.: Experimental 8 MeV synchrotron for electron acceleration.
 2964 Nature 158, 413 (1946)
- 2965 4. Richardson, J.R., et al.: Frequency Modulated Cyclotron. Phys. Rev. 69: 669 (1946)
- 2966 5. Kerst, D. W.: The Acceleration of Electrons by Magnetic Induction.. Phys. Rev., 60, 47-53
 2967 (1941)
- 2968 6. Photo saturne I. ***** TB completed **** Archives historiques CEA. Copyright
 2969 CEA/Service de documentation - FAR_SA_N_00248
- 2970 7. Photo tranche dipole. Credit: CEA Saclay. ***** TB completed *****
 2971 Archives historiques CEA. Copyright CEA/Service de documentation - FAR_SA_N_02826
- 2972 8. Ratner, L.G. and Khoe, T.K.: Acceleration of Polarized Protons in the Zero Gradient Syn-
 2973 chrotron. Procs. PAC 1973 Conference, Washington (1973).
 2974 http://accelconf.web.cern.ch/p73/PDF/PAC1973_0217.PDF
- 2975 9. Vostrikov, V.A., et al.: Novel approach to design of the compact proton synchrotron magnetic
 2976 lattice. 26th Russian Particle Accelerator Conference RUPAC2018, Protvino, Russia (2018).
 2977 <https://accelconf.web.cern.ch/rupac2018/papers/tupsa17.pdf>.
- 2978 Fig. 9.4: Copyrights under license CC-BY-3.0, <https://creativecommons.org/licenses/by/3.0/>;
 2979 no change to the material
- 2980 10. Suddeth, D.E., et als.: Pole face winding equipment for eddy current correction at the Zero
 2981 Gradient Synchrotron. Procs. PAC 1973 Conference, Washington (1973).
 2982 http://accelconf.web.cern.ch/p73/PDF/PAC1973_0397.PDF
- 2983 11. Raugas, A.V. and Wright, A.J.: Betatron tune profile control in the Zero Gradient Synchrotron
 2984 (ZGS) using the main magnet pole face windings. Procs. PAC1977 conference, IEEE Trans.
 2985 on Nucl. Science, VoL.NS-24, No.3, June 1977
- 2986 12. Floquet, G.: Sur les équations différentielles linéaires à coefficients périodiques. Annales
 2987 scientifiques de l'E.N.S. 2e série, tome 12 (1883), p. 47-88.
 2988 http://www.numdam.org/item?id=ASENS_1883_2_12_47_0
- 2989 13. Leleux, G.: Accélérateurs Circulaires. Lecture Notes, INSTN, CEA Saclay (1978)

- 2990 14. Bohm, D. and Foldy, L.: Theory of the Synchro-Cyclotron. *Phy. Rev.* 72, 649-661 (1947).
- 2991 15. Cohen, D. : Feasibility of Accelerating Polarized Protons with the Argonne ZGS. *Review of*
- 2992 *Scientific Instruments* 33, 161 (1962).// <https://doi.org/10.1063/1.1746524>
- 2993 16. Cho, Y., et als.: Effects of depolarizing resonances on a circulating beam of polarized protons
- 2994 during or storage in a synchrotron. *IEEE Trans. Nuclear Science*, Vol.NS-24, No.3, June 1977
- 2995 17. Parker, E.F.: High Energy Polarized Deuterons at the Argonne National Laboratory Zero
- 2996 Gradient Synchrotron. *IEEE Transactions on Nuclear Science*, Vol. NS-26, No. 3, June 1979,
- 2997 pp 3200-3202
- 2998 18. Lee, S.Y.: *Spin Dynamics and Snakes in Synchrotrons*. World Scientific, 1997
- 2999 19. Froissart, M. and Stora, R.: Dépolarisation d'un faisceau de protons polarisés dans un syn-
- 3000 chrotron. *Nucl. Inst. Meth.* 7 (1960) 297.
- 3001 20. Leleux, G.: Traversée des résonances de dépolarisation. Rapport Interne LNS/GT-91-15,
- 3002 Saturne, Groupe Théorie, CEA Saclay (février 1991)
- 3003 21. Bruck H., Debraine P., Levy-Mandel R., Lutz J., Podliasky I., Prevot F., Taieb J., Winter S.D.,
- 3004 Maillot R., Caractéristiques principales du Synchrotron à Protons de Saclay et résultats obtenus
- 3005 lors de la mise en route, rapport CEA no.93, CEN-Saclay, 1958.
- 3006 22. Méot, F.: Zgoubi Users' Guide.
- 3007 <https://www.osti.gov/biblio/1062013-zgoubi-users-guide> Sourceforge latest version:
- 3008 <https://sourceforge.net/p/zgoubi/code/HEAD/tree/trunk/guide/Zgoubi.pdf>
- 3009 23. Foss, M.H., et al.: The Argonne ZGS Magnet. *IEEE* 1965, pp. 377-382, June 1965
- 3010 24. Klaisner, L.A., et al.: *IEEE* 1965, pp. 133-137, June 1965